Influence of sub-atmospheric pressure on flame shape and sooting propensity in ethylene laminar coflow non-premixed flame

R. Jalain, J. Bonnety, A. Matynia, J.M. Citerne, H. Dutilleul, A. Jocher, J.L. Consalvi, G. Legros

To cite this version:

R. Jalain, J. Bonnety, A. Matynia, J.M. Citerne, H. Dutilleul, et al.. Influence of sub-atmospheric pressure on flame shape and sooting propensity in ethylene laminar coflow non-premixed flame. Combustion and Flame, 2023, 259, pp.113173. 10.1016/j.combustflame.2023.113173 . hal-04441785

HAL Id: hal-04441785
https://hal.sorbonne-universite.fr/hal-04441785

Submitted on 6 Feb 2024

Influence of sub-atmospheric pressure on flame shape and sooting propensity in ethylene laminar coflow non-premixed flame

R. Jalain[a,b], J. Bonnety[c], A. Matynia[a], J.M. Citerne[a], H. Dutilleul[a], A. Jocher[d], J.L. Consalvi[e], G. Legros[f]

[a] *CNRS, Sorbonne Université, UMR 7190, Institut Jean Le Rond d'Alembert, Paris F-75005, France*
[b] *DMPE, ONERA Palaiseau, Université Paris Saclay, Palaiseau F-91123, France*
[c] *EM2C, CNRS, CentraleSupélec, Université Paris-Saclay Gif-sur-Yvette 91190, France*
[d] *TUM, School of Engineering and Design, Technische Universität München Boltzmannstr. 15, 85748 Garching b. München, Germany*
[e] *Aix-Marseille Université, IUSTI/UMR CNRS 7343, 5 rue E. Fermi, Marseille, 13453, Cedex 13, France*
[f] *CNRS-ICARE, Univ. Orléans, 1C Avenue de la Recherche Scientifique, 45071 Orléans Cedex 2, France*

Abstract

Sooting flames have been a longstanding research topic and an extensive literature has been developed at both atmospheric and high pressure. In contrast, studies of sooting flames at subatmospheric pressures are relatively scarce. As pressure decreases buoyancy, and consequently buoyancy-driven convective flow, decreases as well. So one could expect characteristic residence times to be longer. To assess the intuitive finding, steady coflow non-premixed ethylene/air flames were established at different pressure conditions, ranging from 0.2 to 1 bar. The configuration was documented by both numerical and experimental works. By the Modulated Absorption Emission (MAE) technique, fields of temperature, soot volume fraction, and dispersion exponent as a measure of soot maturity were extracted. Extending the MAE setup from 2 to 4 spectral ranges allows a more accurate evaluation of the dispersion exponent together with the temperature calibration factor. Numerical simulations were conducted using the CoFlame code, giving access to the flow topology and the governing characteristic times. According to numerical simulations, with increasing pressure, while the buoyancy-driven convective flow does increase, the flow velocities do decrease. It seems consistent with experimental results, finding higher maturity, expected with higher residence time, when increasing pressure. In addition to the important database produced for flames under sub-atmospheric conditions, this paper also couples originally experimental and numerical results, leading to (i) the reconstruction of the synthetic signals that a camera would capture, and (ii) the tracking of the quantities of interest experienced along the streamlines. Most of the global trends are well-captured by CoFlame, i.e. decreasing pressure leads to the decrease of soot volume fraction, maturity, and flame height, together with the increase in temperature. Meanwhile, significant discrepancies can be noticed, i.e. the numerical simulations overestimate the soot volume fraction, especially for the lower pressure levels, together with an underestimated flame temperature leading to an overestimation of the flame height.

Keywords: Optical diagnostics, sub-atmospheric pressure, sooting non-premixed flame

---

1. Introduction

As pointed out by Panek et al. [1], combustion in weakly buoyant or micro-gravity environments is now a crucial branch of combustion science and research. Indeed, fire hazard has been identified as one of the major issues that still obstruct missions to Mars and beyond. In such a scenario, the contribution of soot to radiative heat transfer might influence at a leading order the capacity of the flame to spread [2]. The future of space exploration depends on the safety of space technology, which includes a complete understanding of combustion processes in the absence of buoyancy or in weakly buoyant environments.

For this reason, high-fidelity of numerical simulations developed to capture both the radiative and sooting features of non-premixed flames is crucial. Non-premixed laminar coflow flames are widely used to assess the required features. This flame configuration is complex enough to account for effects such as two-dimensional effects on buoyancy or diffusion as well as various residence times (varying with the radial position at the exit of fuel tube), which one-dimensional configurations that are often used to evaluate soot models do not offer. The application of a two-dimensional computational modeling to coflow flames still allows numerical simulations to include detailed chemical mechanisms, which is often prohibited for a matter of computational cost in turbulent and three-dimensional configurations.

Under normal gravity, a solution that might appear appealing to minimize buoyancy effect is the study of sub-atmospheric sooting flames where the buoyancy is reduced as the pressure decreases. As a result, the characteristic residence times associated with combustion processes should be longer as pressure decreases [1]. Furthermore, these sub-atmospheric conditions can help improve the fundamental understanding of the effect of pressure on soot properties over the full pressure range, i.e. sub- and super-atmospheric pressure ranges.

The effect of pressure p on soot formation in flames is significant and the main trend is understood. Soot concentration increases with pressure. Non-sooting flames at a given pressure can turn into sooting or even smoking flames at higher pressures [3, 4]. That being said, the rate of the increase depends on several characteristics at very different scales, from fuel composition to flame shape or pressure range. Numerous studies have focused on the pressure/soot production relationship [3, 5–16]. In order to characterize the trend, many authors have established a relation of the following type:

$$[soot] \propto p^n \tag{1}$$

where $[soot]$ represents a characteristic quantity such as the maximum volume fraction, $f_{v,max}$, or the maximum conversion of carbon to soot η_s.

Interestingly, Liu et al. [17] found a linear correlation (n=1) from inverse coflow flame, which is significantly different from normal coflow flame where a power law is suitable, underlying the complexity of this relationship.

In the case of normal coflow flame, a large variability of the value attributed to the exponent n, depending on the fuel (for a given pressure range) but also on the pressure range. For example, n is 1.61 for an ethane flame over the 2-10 bar range [18], then 1.08 for the 10-15 bar range [18]. A similar reduction in the value of n can be observed for methane [7]. Thus, there would be a global decrease in the growth of the propensity to produce soot with the increase of pressure [19]. Generally, it seems that the peak local soot volume fraction $f_{v,max}$ increases with pressure then tends to an asymptotic constant where it becomes invariant with p. In other words, the rate of increase of $f_{v,max}$ would decrease as the pressure increases [19]. Consequently, a higher sensitivity of the aforementioned rate is expected at sub-atmospheric levels of pressure, further consolidating the development of numerical models, especially for non-premixed flames [20–28].

For these reasons, flames established at sub-atmospheric range of pressure have been paid much attention [1, 29–33]. Beyond sooting propensity, several comments on the physics of the flames can be reminded.

First of all, over this range of conditions, the experimental constraints get less stringent, non-premixed flames being easier to stabilize. Secondly, temperature usually decreases in the sooting area when the pressure increases due to more important radiative heat losses [7, 27, 31, 34].

Concerning the flame shape, increasing pressure conditions increase chemical reaction rates and causes the expanding hot gases to accelerate more rapidly, enhancing the transport of fresh oxidizer to the reaction zone [31]. As a result, the reaction zone narrows and the flame radius R_f decreases [3, 6, 7, 35]. To respect the mass conservation $\dot{m} = \rho v A$, as the density ρ scales with p^1, the velocity v varies as a function of the cross-section area $A = \pi {R_f}^2$. Letting $R_f \propto p^{-a}$, if $a = 0.5$, v would remain constant while it would increase or decrease with pressure if a stands below or beyond 0.5, respectively [36]. Experimental measurements [3, 7–9, 12] and numerical predictions [37] of soot volume fraction found that the flame diameter was proportional to $p^{-1/2}$. These findings tend to attest that the residence time is independent of p for constant fuel mass flow rates. Numerically, Liu et al. [37] showed that the axial velocity along the flame centerline was nearly pressure-independent. In contrast, the numerical investigations by Charest et al. [31] found that the residence time increases with the increase of pressure and they attributed this trend to the fact that the flame diameter was in fact proportional to $p^{-0.4}$.

Although flame diameter decreases with increasing pressure, Roper's correlations for buoyancy-dominated laminar jet non-premixed flames [38] state that the visible flame height, to a first-order approximation, is independent of pressure and depends on mass flow rate only. However, several studies [3, 6, 7, 35] have observed pressure-dependent flame heights during experiments involving laminar non-premixed flame. These experiments generally showed that the visible flame height initially increased at a lower pressure range then remained constant over a central range [8, 9] and finally decreased at a higher pressure range. On the contrary, constant flame heights were numerically predicted by Liu et al. [37]. For methane/air flame, Charest et al. [34] predicted an increase with the pressure of height over the range 1-20 atm then a constant height over this threshold. The authors admitted that the origin of this increase in flame height is not clear since the flames are all buoyancy-controlled (Froude number $\ll 1$) within the range of pressures studied. For ethylene/air, Charest et al. [31] also predicted an increase of height with pressure over the range 0.5-5 atm and suggested that the ethylene flames studied were still developing and not fully buoyancy-dominated, even at 5 atm.

In an effort to combine both the experimental assessment of the trends examined above and associated numerical diagnostics, a new experimental setup has been designed to probe sub-atmospheric non premixed ethylene/air flames with the non-invasive Modulated Absorption Emission (MAE) technique [39, 40] while these flames are simulated by the CoFlame code [25]. To further document the history throughout the flame of characteristics associated with soot morphology, the optical setup has been upgraded from 3 [41] to 4 spectral ranges. Spatially-resolved information are then obtained on volume fraction, temperature, and now also on dispersion exponent of soot α, commonly called Ångström exponent, a quantity related to soot maturity [42–44].

2. Initial experimental observation

A set of flames is investigated, i.e. 9 flames ranging from 0.2 bar (E02) to 1 bar (E10) by step of 0.1 bar with a constant ethylene mass flow rate of 4 mg/s and a constant air mass flow rate of 30 nl/min. These closed-tip flames, stabilized on a Santoro burner (fuel outlet diameter $d_F = 11$ mm), can be observed in Fig. 1.

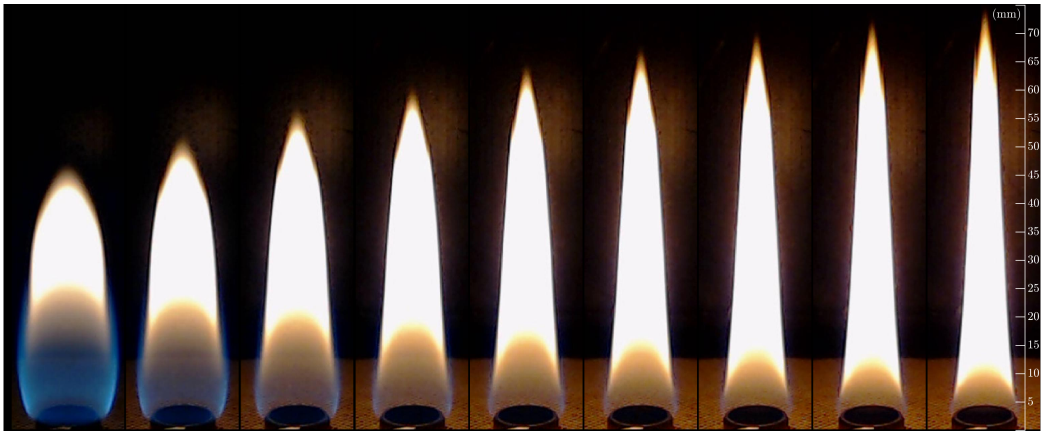

Figure 1: Pictures of the investigated flames. From left to right the pressure varies from 0.2 bar (flame E02) to 1 bar (flame E10).

From this straightforward visualisation, one can see that the flame height H_f increases with pressure while the flame radius R_f decreases (E10 is roughly 1.5 times higher than E02). This observation is consistent with literature [3, 6, 7, 32, 35, 45] as pointed out in the introduction. Intuitively, one could think that this increase comes from the increase of the buoyancy-driven convective flow which accelerates the flow and thus stretches vertically the flame. Charest et al. [31] showed that in the case of sooting flames, energy exchanges, especially radiation, between soot particles and gas have an incidence on the height variation. In contradiction with Roper's correlations for buoyancy dominated laminar jet non-premixed flames [38], the aforementioned trend suggests that more than two quantities, i.e. the exit velocity v and the molecular diffusion D, are necessary to predict the height of coflow sooting flames. Buoyancy, soot concentration and gas absorption are expected to decrease with decreasing p. This leads to a reduction of radiative losses and potentially to increase the temperature. Therefore, to adress the evolution with p of the flame shape, at least f_v and T need to be known.

On the other hand, nascent and mature soot particles have significantly different properties, appearances, and internal nanostructures. The surface of nascent soot is considerably more reactive than that of mature graphitized soot [46–49]. As a consequence, the time to fully oxidize a soot particle can vary greatly and the evaluation of the maturity is also a valuable asset.

3. Hardware and methods

3.1. Flame generation

A Santoro burner is located inside a newly designed pressure-regulated chamber, displayed on Figs 2 (a) and (b), with an internal diameter of 160 mm. This diameter is sufficient to ensure an undisturbed fluid flow: (i) the walls do not heat up during the experiments, (ii) the cross-section reduction at the top end of the chamber is far enough from the flame to maintain a laminar regime over the whole measurement area. The chamber has 4 rectangular quartz optical ports of 100 mm by 40 mm. The pressure is controlled by a Bronkhorst EL-PRESS electronic controller which includes the sensor, the control valve and the PID loop. A vacuum pump (DVP SB 40) is used for pressure reduction and a reagent accumulation for pressure increase. An additional air flow runs through the chamber from its base, to avoid any accumulation or recirculation. The regulation consists in keeping the leakage flow necessary to maintain the pressure, which is stabilized to the accuracy of one millibar (the measurement oscillates only between 3 levels of the sensor, i.e. 0.33 mbar). A rupture disk set to break at 11 bar provides additional safety.

Fig. 2 (c) shows the different elements and dimensions of the burner. The oxidizing mixture is introduced through an annular section. Upstream of the outlet, the coflow is composed of a bed of glass beads with a diameter of 3 mm and a ceramic honeycomb. In the center of the ring is a brass tube of effective diameter $d_F = 11$ mm and a thickness e of 1 mm which ensures the passage of the fuel. This reference diameter is identical to Refs. [50, 51]. The outlet section of the central tube is located 4 mm above the annular flow's one, allowing the latter to establish itself in laminar regime before encountering the fuel. The tube was temperature regulated at 313 K by 3 heating cartridges. The burner can be moved vertically so that the flames can be probed entirely by optical techniques through the windows.

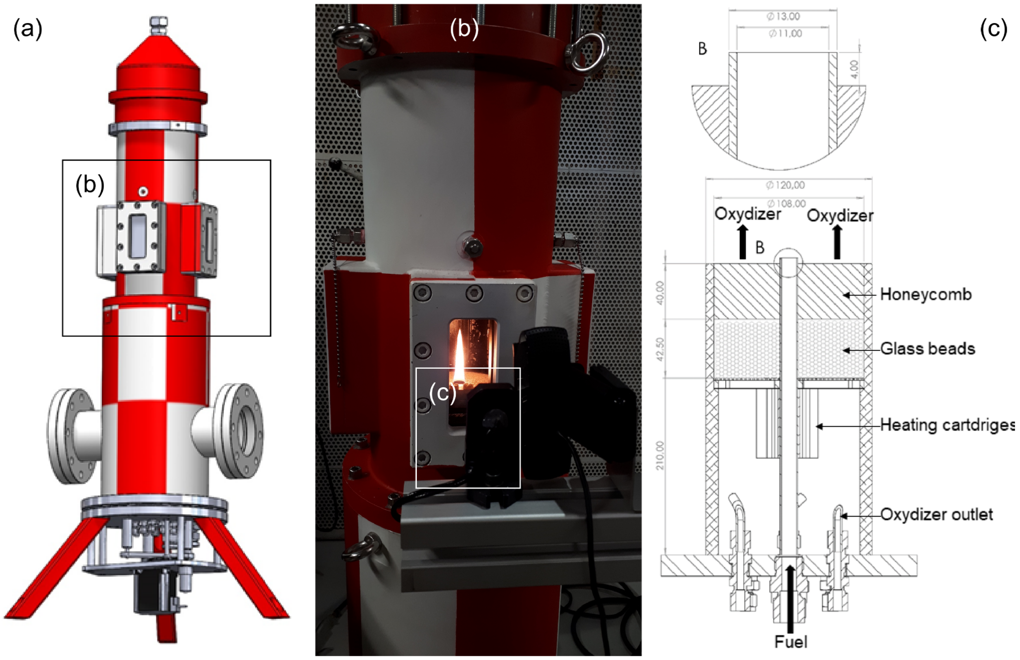

Figure 2: (a) 3D-view of the combustion chamber; (b) Picture of the burner with a photodiode (left) and a webcam (right); (c) Burner dimensions and elements.

3.2. Experimental diagnostic

An MAE setup allows both, the line-of-sight light extinction (evaluated in terms of light transmissivity τ) and the integrated flame emission (P_λ) to be measured within each of the four detection spectral ranges identified in the following by their centres: 430 nm, 450 nm, 580 nm and 645 nm. The latter two are expected to be hardly affected by the scattering contribution and the PAH absorption to extinction or by chemiluminescence regarding emission. On the contrary, the former two ones might be affected by these phenomena: a higher scattering contribution, a higher PAH absorption, and chemiluminescence from CH^* and C_2^* (revealing around 430 and 450 nm, respectively). However, they are necessary to obtain the dispersion exponent α and to consolidate the calibration factor value γ_λ used to retrieve the soot temperature T. The scattering effect is discussed in the Supplementary Material, while chemiluminescence is expected to be located outside of the soot region [52] and at a far lower level than blackbody radiation associated with soot. Capturing selectively these signals is ensured by different filters whose characteristics are presented in Fig. 3.

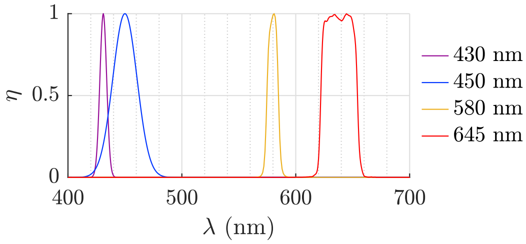

Figure 3: Transmission of the filters.

The optical setup is presented in Fig. 4. A LED panel (1) is used as light source, emitting from 400 to 800 nm. Its power can be adjusted and has been set to obtain the highest signal just below the saturation of the camera sensor when both the flame emission and the light attenuated through the flame are captured together.

After passing through the flame (2), the light goes through an achromatic lens (3) which makes the light beam convergent to a focal point where a pinhole (4) with an aperture diameter of 500 ± 5 μm is located. Then, a Hamamatsu lens ($f = 50$ mm, $F/D = 3.5$) images the flame on the photocathode of a V4183U-02 Hamamatsu image intensifier. After being amplified and re-imaged at a monochromatic wavelength thanks to a relay lens, the light is finally collected and digitized by the 16 bits sCMOS sensor (5) of a pco.edge 5.5 camera at a wavelength where the quantum efficiency is maximum (530 nm).

The image intensifier gives a better dynamic on extinction and emission measurements. The small pinhole aperture leads to the collection of mainly parallel beams. The optical arrangement formed by the achromatic lens, the pinhole, and the camera lens provides a telecentric lens configuration. This depth invariant magnification filters the parallax error and the beam steering effect on the flame edge due to the strong temperature gradient. Consequently, the optical arrangement ensures a reliable line-of-sight interpretation on the mapped area, i.e. 100×40 mm with a resolution of 76 μm by pixel.

To obtain the set of 4 frames required by the MAE technique, a pulse generator switches ON and OFF the LED panel, the intensifier and the camera acquisition to a rate of 10 Hz, with the flame (I) and without the flame (I_0). To improve the signal-to-noise ratio, 200 images of every steady flame were recorded and averaged.

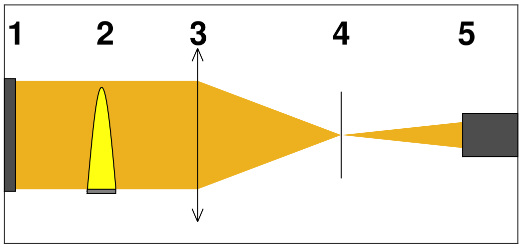

Figure 4: Optical setup with (1) LED pannel (2) Flame (3) Converging lens (4) Pinhole and bandpass filter and (5) intensifier and camera.

On every pixel and for a given spectral range, the integrated extinction K_λ is then expressed as follows:

$$K_\lambda = -\log(\tau) = -\log\left(\frac{I_{f,l} - I_f}{I_l - I_b}\right) \tag{2}$$

with τ the transmissivity within the spectral range, $I_{f,l}$ the intensity of the averaged frame with flame and light on, I_f that with flame only, I_l that with light only, and I_b the background signal (without flame and light).

The line-of-sight integrated emission P_λ is expressed as:

$$P_\lambda = I_f - I_b \tag{3}$$

3.3. Numerical diagnostic

The numerical code CoFlame [25] has been used for modelling the set of flames investigated. For the gaseous phase, the fully coupled elliptical conservation equations for mass, momentum, energy, and species mass fraction are solved within the low Mach number approximation. CoFlame utilizes the axisymmetric nature of the flame, and equations are solved in the two-dimensional (z and r) cylindrical coordinate system. As the original publication of CoFlame, the kinetic mechanism (94 species and 831 reactions), originally developed by Slavinskaya et al. [53] is used.

Soot particle dynamics are described using a fixed sectional method, in which soot particle mass ranges are divided logarithmically into thirty-five discrete sections. Thirty-five sections are sufficient to ensure the results for average soot morphological parameters no longer change when increasing the number of sections. Soot aggregates are assumed to be composed of spherical primary particles of equal size with a constant fractal dimension of 1.8.

Soot particle nucleation is modeled by assuming soot nucleates through the collision and sticking of PAH species. The nucleation species are benzo[a]pyrene (BAPYR), secondary benzo[a]pyrenyl (BAPYR*S), and benzo(ghi)fluoranthene (BGHIF). Inception efficiency β was set to 0.0001, coagulation efficiency ξ to 0.2.

The PAH condensation model utilized is based on transition and continuum regime collision theory between soot aggregates and PAHs, with a collision efficiency of 0.85. The HACA surface growth and oxidation model utilized is based on the HACA and oxidation soot surface reaction scheme developed by Frenklach and coworkers [54, 55]. Six surface reactions are considered. 5 of them are described using the concept of soot surface sites, which can either be saturated or dehydrogenated.

The original soot oxidation sub-model [25] is used. It includes two species for soot oxidation, i.e. OH and O_2. Neoh et al. [56] found experimentally that generally OH dominates soot particle oxidation but O_2 can become significant, especially at lower temperatures. Comparing soot oxidation measurements and model rates from literature, Guo et al. [57] concluded that the predicted model rates are generally higher than the measured ones.

The coupling with the Radiative Transfer Equation is solved following the discrete-ordinates method (DOM) combined with a statistical narrow-band correlated-k-based model that includes the contributions of soot, CO_2, H_2O, and CO [58].

9 flames are then computed at pressure p ranging from 0.2 bar (N02) to 1 bar (N10) by step of 0.1 bar. Like the Santoro burner, the inner diameter of the central fuel tube is 1.1 cm. For a given flame, the fuel and air velocities are set to $\frac{5}{p/p_0}$ cm/s and $\frac{5.5}{p/p_0}$ cm/s ($p_0 = 1$ bar), respectively. The computational domain, extending to 19.6 cm in the axial direction z and 4.16 cm in the radial one r, is divided into $384(z) \times 110(r)$ non-uniform control volumes. As prescribed in the original publication, the first 1.0 cm in the z-direction stands below the fuel tube exit plane. This distance is sufficient to ensure the temperature gradients throughout the flow at $z = 0$ mm are negligible, thus ensuring consistent boundary conditions. The outer radial boundary corresponds to a radius smaller than the oxidizer tube radius, which leaves the oxidizer tube wall out of the computational domain. The resulting flames are all non-smoking with a closed-tip.

From the numerical data are extracted the fields of soot oxidation rates by O_2 and OH, the formation rates by condensation and HACA, the inception rate, soot volume fraction f_v, temperature T, C_2H_4 and O_2 molar fractions

X, radial velocity v, and axial velocity u. From these velocities, streamlines and travel time t can be computed. On these streamlines, two more quantities are used (i) the formation time t_f as the time from when the volume fraction along the streamline reaches 0.1 ppm to the time when the volume fraction along the same streamline decreases and, (ii) the oxidation time t_{ox} starting from the same point to the time when the volume fraction along the streamline reaches 0.1 ppm again. Fig. 5 displays these quantities on the Flame N10.

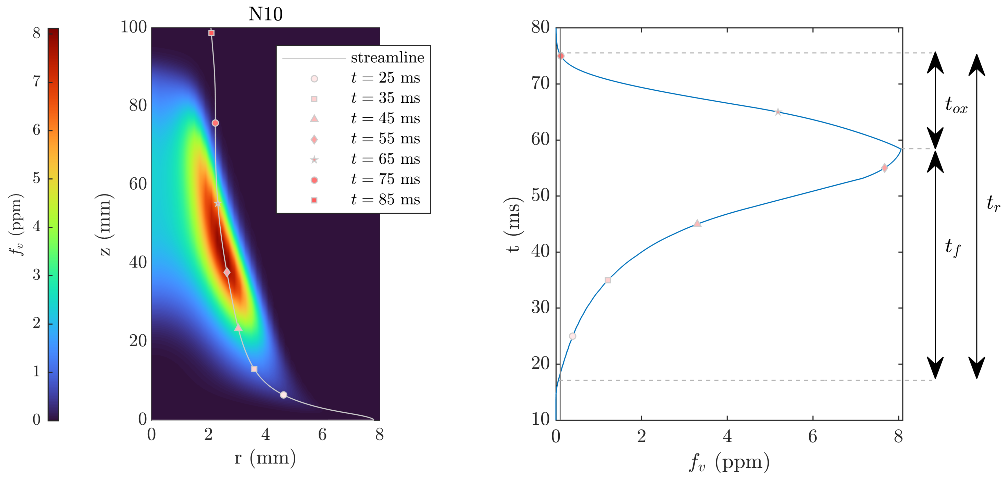

Figure 5: Left: a streamline passing through N10 f_v field with markers separated by 10 ms. Right: f_v along the streamline as a function of time t.

4. Results

4.1. Soot concentration and sooting tendencies

As a line-of-sight technique, the MAE is combined with a subsequent deconvolution to obtain the local extinction coefficient distribution $k_{ext,\lambda}(r, z)$. The deconvolution is done by onion-peeling rather than Abel Three-Point inversion and incorporates a Tikhonov regularization [40]. The resulting coefficient is mainly governed by the contribution of the local absorption coefficient κ_λ and augmented by a portion σ_λ attributed to scattering. This leads to the following expression:

$$k_{ext,\lambda}\,(r, z) \;=\; (1 + \sigma_\lambda)\,\kappa_\lambda(r, z) \tag{4}$$

where r is the radial distance from the flame axis, z the Height Above the Burner (also referred to as HAB), and σ_λ is the ratio of the scattering coefficient to the absorption one at a given wavelength λ.

While it is noticed that the scattering contribution to the extinction is increasingly important with decreasing wavelength, absorption by soot particles is shown to be at least one order of magnitude higher than scattering in the spectral range investigated [42]. More details about the evaluation of scattering can be found in the Supplementary Material. Scattering is here neglected and the soot volume fraction f_v is determined by assuming the Rayleigh limit of the Mie theory for the whole set of flame:

$$f_v = \frac{\lambda}{6\,\pi\,E(m_\lambda)}\,\kappa_\lambda \tag{5}$$

with $E(m_\lambda) = -\Im\left\{\frac{m_\lambda^2-1}{m_\lambda^2+2}\right\}$, the function of absorption and $m_\lambda = n - ik$ the complex index of refraction.

Additionally, as defined in Ref. [59], the soot load F_v along the flame's axis can be computed as follows:

$$F_v(z) = \frac{1}{\pi R^2}\int_0^R 2\pi r f_v(r, z)\mathrm{d}r \tag{6}$$

In Ref. [59], R was set to the fuel tube radius $\frac{d_F}{2}$. However, in the current study, some flames extend radially beyond the tube radius, so restricting R to this value would result in the integration of truncated profiles. Consequently, R has been set here to the maximum radius where extinction is detected throughout the whole set of flames.

The soot load allows to distinguish the heights where soot formation is more important than oxidation, below $F_{v,max}$, from the heights where the relative importance of the two phenomena are reversed, above $F_{v,max}$. Consequently, it can be considered as a relevant characteristic of the competition between soot formation and oxidation along the globally upward trajectories that any particle experiences.

The soot volume fraction fields are computed with the absorption measurements obtained at 645 nm, since the scattering is expected to be as low as possible given the spectral range enabled by the collection setup. A constant $E(m_\lambda) = 0.2645$ is selected to match the peak soot volume fraction $f_{v,max}$ throughout the computed flame N10. This value is consistent with the literature that reports a range from 0.2066 [60] to 0.42 [42]. Flame 10 is the closest flame to Santoro's NS flame [61], one of the references for the development of CoFlame. Flame 10 ethylene flow rate is slightly lower than NS flame. Fig. 6 presents on the left the experimental (E02-E10) and numerical (N02-N10) soot loads F_v as a function of the HAB z with the dashed lines showing the evolution with the pressure of $F_{v,max}$ location. On the right are displayed the fields of soot volume fraction f_v for every flame. Values below 0.1 ppm are deliberately not displayed (experimentally and numerically), being too close to the detection limit of the optical setup. Some careful interpretations can be achieve for f_v<0.3 ppm but at the expense of significantly increased noise.

The soot volume fraction presents a overall fairly good agreement between the numerical and experimental fields. However, discrepancies are observed at lower pressures where higher volume fractions are predicted.

We observe that numerically the soot wings extend higher and the flame tip is also higher. These discrepancies have been previously observed in the literature [25, 62]. While experimental measurements on the Santoro flame [61] report about 1 ppm at $z = 8$ cm, the CoFlame simulation still calculates 6 ppm. Since soot growth leads to similar $f_{v,max}$, it would thus seem that the soot oxidation rate is underestimated. Concerning this point, Smooke et al. [62] attributed this deficiency, in the case of their model, to the formation of primary particles much larger than the typical maximum experimental values ($d_p \approx 25$ nm). These large particles slowed down the oxidation process and are responsible for the extension of the subsequent wings. In practice, the primary soot particles reach a maximum size due to the deactivation of the active surface (aging). Concerning CoFlame, from our understanding of the models, this phenomenon is already taken into account by the HACA surface

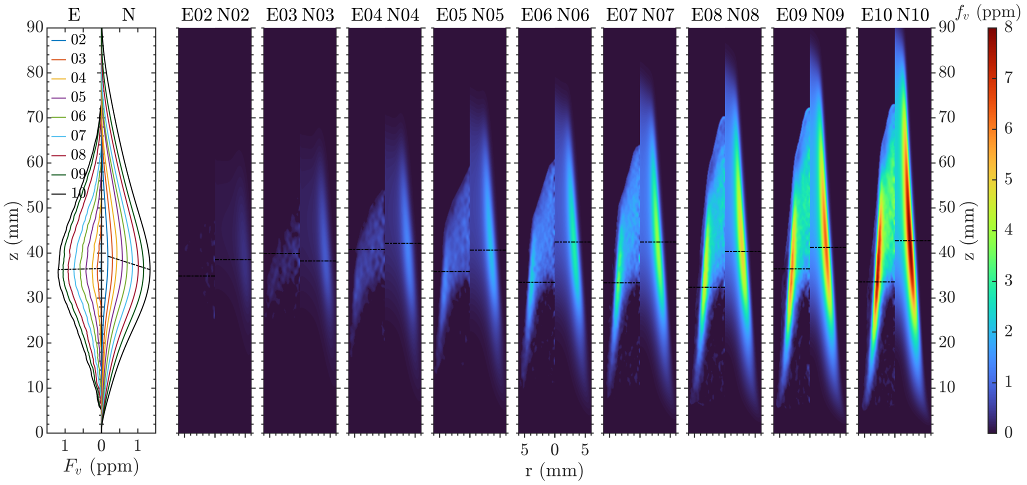

Figure 6: Left: evolution of the soot load F_v as a function of the HAB z within experimental (E02-E10) and numerical (N02-N10) flames. The locations of $F_{v,max}$ are connected by the dashed lines. Right: Corresponding fields of local soot volume fraction f_v with the location of $z = f_{v,max}$ (dashed lines).

growth and oxidation model that uses the concept of soot surface sites, which can either be saturated or dehydrogenated. However, in the case of the N10 flame, the average diameters of the primary particles are close to 50 nm and they exceed 25 nm in most of the conditions. This probably partly explains the extension of the wings.

Secondly, in the lower regions of the flames, where the volume fraction along the symmetry axis is zero (around $z < 30$ mm), the numerical radial profiles are more spread out than the experimental profiles. However, in this area, the numerically calculated f_v levels are higher than 0.1 ppm, thus beyond the detection limit of optical diagnosis. If these concentrations were effective, the optical setup would have measured them. Therefore, it would appear that the numerical modeling does overestimate the width of these profiles.

Finally, above $f_{v,max}$, experimentally, the core of the flame (between the axis of symmetry and the f_v peak) always indicates higher levels of soot volume fraction. If this discrepancy comes from an experimental bias, it can be attributed to two phenomena: (i) an overestimation of the absorption in the extinction (because scattering is considered negligible) and (ii) an important spatial evolution of $E(m_\lambda)$ (spatially constant here). We can estimate the contribution of these two potential biases:

- (i) neglecting scattering, especially for areas containing large aggregates where Rayleigh-Debye-Gans scattering theory for fractal aggregates (RDG-FA) would be more appropriate (but requires more assumptions) than Mie theory in the Rayleigh regime. However, references [42, 43] found that, in a configuration similar to the E10 flame, in the region under consideration, i.e., the core of the flame, the scattering around 500 nm is expected to be far less than 5% (thus even lower at 645 nm). It cannot, therefore, be responsible for the large discrepancy observed.
- (ii) the same studies have shown that $E(m_\lambda)$ is higher in the wing than in the core, which would lead to even smaller differences between the peak and the f_v of the central line.

The underprediction of the soot volume fraction in this area (high z, low r), at atmospheric pressure, has been observed for many different soot formation models in the literature. The cause of the observed underprediction may be due to unmodeled physical phenomena or formation pathways leading to increased soot growth rates along the centerline of non-premixed flames [25]. The data collected here suggest the same issue for sub-atmospheric pressures.

Concerning the soot load F_v, the left part of Fig. 6 shows the evolution with the height of the experimental (left) and numerical (right) F_v soot load as a function of the pressure. Only the cases where f_v is detected are shown.

Comparing the numerical and experimental profiles of F_v, the localization of $F_{v,max}$ as a function of pressure is well reproduced: a slight shift to a lower position with the increase of pressure. Numerically F_v starts to grow slightly lower and the $F_{v,max}$ is always obtained slightly higher. The distance along z to obtain $F_{v,max}$ is then longer. On the other hand, in the part where soot oxidation prevails, i.e., above the location of $F_{v,max}$, the experimental decrease of F_v is steeper than the numerical decrease. Thus, it appears that numerically, the formation/oxidation balance is slightly too much in favor of formation regardless of height. Comparing the evolution of $F_{v,max}$ values, the increase with pressure seems linear, both experimentally and numerically.

The quantity $f_{v,max}$ is used as a metric to investigate the effects of pressure on soot propensity as done in previous works [7, 18, 19]. In addition, the location where this peak value occurs, referred to as $z(f_{v,max})$ is also compared with the experimental one. Fig. 7 displays the experimental profiles f_v (left), the numerical ones (middle), and $f_{v,max}$ as a function of pressure (right). By comparing the profiles, the numerical flames seem extremely consistent with the experimental ones (value and position), except for the flames below 0.6 bar, where experimental $f_{v,max}$ are lower. This suggests that for the upper part of the visible spectrum and for significant f_v (i.e. greater than 1 ppm), keeping $E(m_\lambda)$ spatially constant seems relevant. We also observe a shift of the peak towards the center of symmetry of the flame, due to the decrease of the diffusion with pressure. Here the radial position evolves with $p^{-0.5}$.

Additionally, an interesting feature about the radial profile shape can be noticed, i.e. a transition from a clear peak to a more continuous level of f_v when decreasing the pressure, with a clear threshold at 0.4 bar. This dynamic is similar to the one observed in Refs. [42, 62] where dilute ethylene flames were studied. This is not reproduced by the numerical flames.

The maximum local soot volume fraction evolves with pressure as follows:

$$f_{v,max} \propto p^n \propto p^{2.4} \tag{7}$$

This value is higher than some papers in the literature [5, 6], where it was found $n = 2$, and $n = 1.7$ for the pressure range 1-10 atm, and 1-16 atm, respectively. On the other hand, it is lower than the value obtained in Ref. [63]. Karataş and Gülder studied an ethylene flame subjected to a pressure ranging from 1 to 7 bar and assigned to n the value of 2.8.

In conclusion, for a non-premixed ethylene flame subjected to a pressure of 0.2 to 1 bar, the maximum volume fraction $f_{v,max}$ would be proportional to the pressure at power $n = 2.4$. Concerning the integrated quantities $F_{v,max}$ or η_s the dependence with pressure seems linear.

From this significant increase in soot concentration with pressure will result in an increase in soot radiative heat losses which should modify the flame radiative signature and the soot temperature.

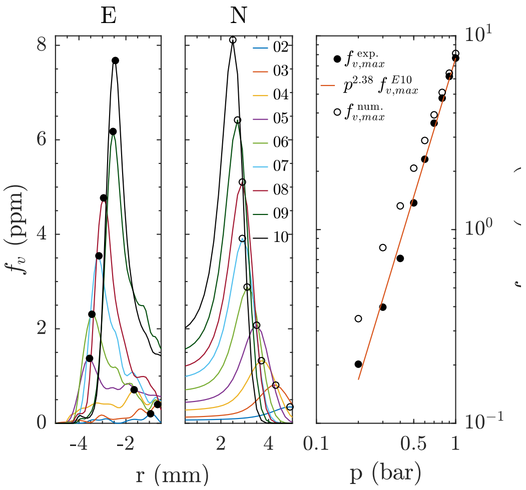

Figure 7: Experimental (left) and numerical (middle) radial profiles at $z(f_{v,max})$ as a function of the pressure. Right: evolution of experimental and numerical $f_{v,max}$ with pressure.

4.2. Radiative signature

From experimental measurements and quantities computed by CoFlame, the radiative signature of the flames can be used to obtain the visible flame contour, temperature field and radiative heat losses.

From experimental data, soot temperature is inferred from MAE procedure, described in detail in Refs. [39, 40]. To this end, emission and absorption are required at two distinct wavelengths. The blackbody radiative intensity B_λ attributed to soot depends on T and soot is assumed to be at the thermal equilibrium with the gas phase.

The flame radiative intensity emitted and partially self-absorbed by soot particles (P_λ) for a given narrow range of wavelength centred on λ represents the local soot emission integrated along line-of-sight (l) leading to the photodetector and can be expressed as follows:

$$P_\lambda\,(L,T) = \int_L J_\lambda\, e^{-\int_l \kappa_\lambda(l)\,\mathrm{d}l}\mathrm{d}l \tag{8}$$

with J_λ the local soot emission, obtained by deconvolution of P_λ. The exponential term in Eq. (8) represents the self-absorption along the remaining flame path (l) to the photodetector. J_λ is defined as follows :

$$J_\lambda = \frac{1}{\gamma_\lambda}\kappa_\lambda\, B_\lambda \tag{9}$$

with γ_λ an absolute calibration factor depending of the camera factor response and the optical arrangement for the collection, κ_λ the local absorption coefficient considered spectrally constant for the narrow spectral range, and B_λ the blackbody radiative intensity given by Planck's law, integrated over the transmission band of a given filter:

$$B_\lambda = \int_{\Delta\lambda} \eta\, \frac{2h\pi c^2}{\lambda^5\left(e^{\frac{hc}{\lambda kT}}-1\right)}\mathrm{d}\lambda \tag{10}$$

with η the transmittance through the filter at the wavelength λ, c the speed of light, k the Boltzman constant, h the Planck one and T the temperature.

The blackbody intensity field $B_\lambda(T)$ can be ultimately inferred as follows:

$$B_\lambda(T) = \gamma_\lambda \frac{J_\lambda(r,z)}{\kappa_\lambda(r,z)} \tag{11}$$

4.2.1. Visible flame contour

To evaluate the flame shape, two quantities are generally used, i.e. stoichiometric flame front or (see Supplementary Material) visible flame contour (of iso-intensity). The first one is easy to obtain numerically while the second can readily be extracted experimentally but can also be evaluated numerically.

In case of sooting flame, f_v peak location has been used as well by Charest et al. [31] since it is correlated with visible emission [35]. In this type of flame, over the upper part of the visible spectrum ($\lambda > 550$ nm), the continuum of blackbody radiation is by far the main contribution of the visible light and consequently visible flame contour can be evaluated by the blackbody radiation obtained numerically with f_v and T fields.

To compute the visible light emitted from the flame due to soot radiation, the integrated emission P_λ must be computed. The first step is to obtain J_λ (Eq. (9)). The computations are made at 645 nm, i.e. the highest wavelength used experimentally because it gives the highest blackbody intensity for the range of flame temperature considered. κ_λ is obtained from the numerical f_v field (see Eq. (5)) with a value of $E(m_\lambda)$ of 0.2645. From the numerical T field, B_λ is computed by Eq. (10). The second step is the convolution of the field by reverse onion-peeling to obtain the integrated field P_λ. Doing so, the experimental field P_λ (see Eq. (3)) and the numerical one can be compared. The intensity scale of the camera is then normalized to yield an arbitrary unit (a.u.) having the same maximum value as the numerical flame.

From the P_λ field, contours of iso-intensity are defined. The flame height H_f is defined as the higher z coordinate of this contour along the symmetry axis ($r = 0$). The flame radius is the r coordinate of this contour at a given z. Using P_λ allows the comparison with a straightforward and relevant experimental measurement. Additionally, since soot concentration is correlated with visible emission [35], it allows to observe discrepancies between experimental and numerical results, potentially without the knowledge of the f_v field. Moreover, as illustrated in the supplementary material, the method is robust since the spatial variation of $E(m_\lambda)$ or the value of the threshold to obtain H_f does not impact significantly the value of the height or the radius and does not affect the relative trends attributed to the pressure variation.

Fig. 8 presents the result of this computation for the whole set of flames investigated. The left part of each flame is the experimental emission P_λ field. The right part is the numerical one. Firstly, a good agreement is ob-

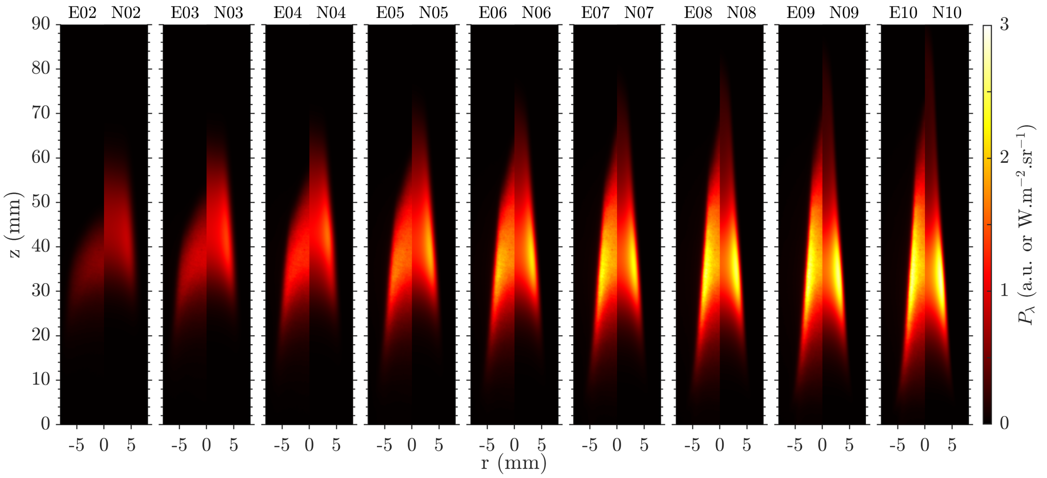

Figure 8: Evolution of the integrated emission P_λ with the pressure for experimental (E02-E10) and numerical (N02-N10) flames.

tained concerning the variation of the maximum intensity value, even if the prediction tends to overestimate it for the lowest pressure. Some discrepancies can also be pointed out, the most striking being the experimental bright area that is always more spread radially. Numerical flames start and close higher.

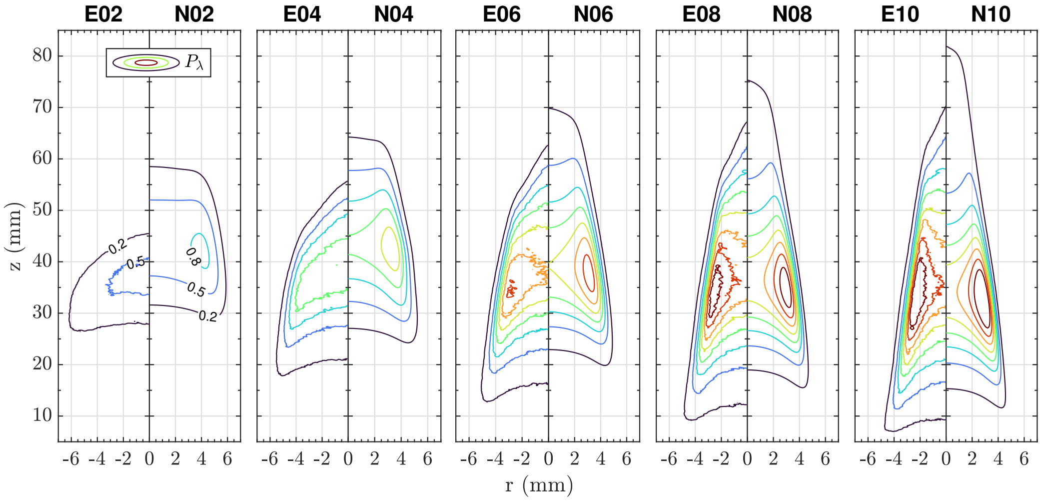

Figure 9: Evolution with the pressure of P_λ contours for experimental (E02-E10) and numerical (N02-N10) flames.

To discuss more precisely these discrepancies, Fig. 9 displays the evolution with pressure of some contours of iso-intensity. Several interesting comments can be given. For higher pressure conditions, the peak of intensity is well located both radially and axially. When the pressure decreases the most intense area moves higher numerically (from roughly $z = 35$ mm to $z = 42$ mm) while it remains constant ($z = 35$ mm) experimentally. More importantly, while the most intense area remains in the wing of the flame numerically, experimentally this area spreads toward the symmetric axis below 0.5 bar. This can mainly be attributed to the soot volume fraction spatial distribution discrepancies observed in the previous section.

Concerning the flame's part above the intensity peak, numerically each contour displays the characteristic wing-shape of an ethylene flame (except the less intense one), slightly shifted inwards with increasing z, then a decrease toward the axis less and less pronounced with decreasing intensity and pressure. On the contrary, experimentally the characteristic wing-shape quickly vanishes and is only visible for high pressure and high value of P_λ.

Concerning the flame shape, by using the less intense contour (black - 0.2), qualitative remarks, as well as quantitative results, can be given. First, there is a good agreement concerning the outermost radial position of the contour from roughly $r = 5$ mm at 1 bar to $r = 6$ mm at 0.2 bar. Concerning the part of the flame below the intensity peak the contour is higher numerically suggesting here an underestimation of the temperature since numerical $f_v > 0.1$ ppm occurs at similar to lower z than experimental ones. Finally concerning the flame tip, first, its location is systemically overestimated numerically. Secondly, at 1 bar, going up, the contour can be described as two segments, one forming an angle of 4° with the vertical axis then a second forming an angle of 9° whereas when pressure decreases, the flame tends to have a constant curvature where it becomes difficult to split it into two segments and the angle between the vertical axis and the contour increases from 9° at 1 bar to almost 90° at 0.2 bar. On the contrary, numerically the two segments can always be drawn and the angle between the vertical axis and the contour is always wider.

To conclude this section, Fig. 10 displays the evolution of the normalized height H_N and radius R_N with pressure, computed with the outer contour (0.2). The evolution between the experimental and the numerical ones changes significantly. While experimentally the increase scales with $p^{0.3}$ (or logarithmically), numerically a linear regression follows more faithfully the trend. Additional measurements can help to understand this discrepancy, i.e. temperature and a maturity indicator.

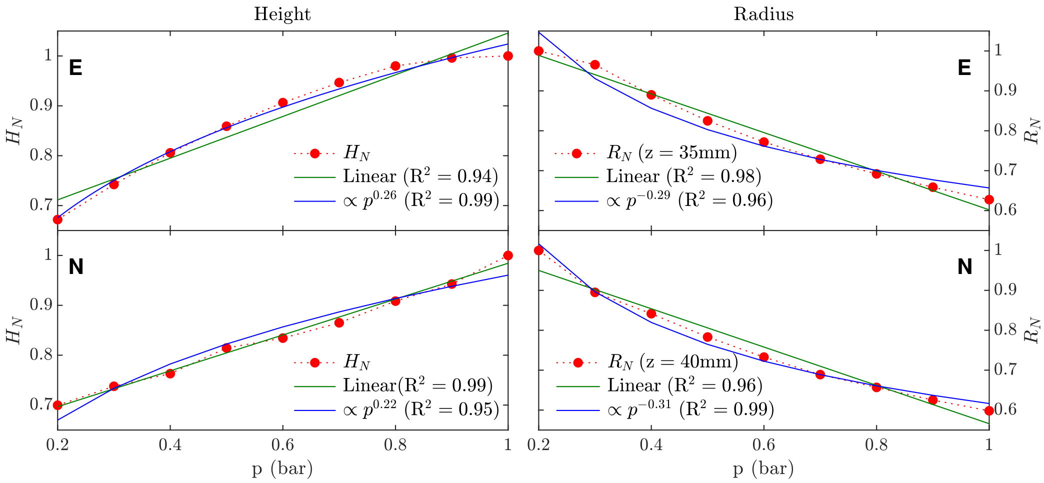

Figure 10: Evolution of the flame height and radius (normalized by the maximum value) with the pressure for experimental (E02-E10) and numerical (N02-N10) flames.

4.2.2. Flame temperature

The absolute coefficient factor γ_λ being quite challenging to determine experimentally, a more convenient procedure is first to use a relative calibration factor $\chi_{\lambda_1/\lambda_2}$ to link the intensity lamp $I_{\mathrm{lamp},\lambda}$ collected in an arbitrary unit from the camera to the absolute radiance given by a calibrating lamp Ocean Optics HL-3 plus CAL:

$$\frac{I_{\mathrm{lamp},\lambda_1}}{I_{\mathrm{lamp},\lambda_2}} = \chi_{\lambda_1/\lambda_2} \frac{\int_{\Delta\lambda_1} \eta B_{\mathrm{lamp}} \mathrm{d}\lambda}{\int_{\Delta\lambda_2} \eta B_{\mathrm{lamp}} \mathrm{d}\lambda} \tag{12}$$

Once the calibration factor $\chi_{\lambda_1/\lambda_2}$ is determined, a look-up table is computed linking the variation of theoretical blackbody emission (Eq. (10)) ratio to the temperature:

$$\omega(T) = \chi_{\lambda_1/\lambda_2} \frac{B_{\lambda_1}(T)}{B_{\lambda_2}(T)} \tag{13}$$

The local temperature $T(r, z)$ was then inferred from the experimental ratio $\omega(T)$ using the expression of the blackbody intensity formulated at two wavelengths:

$$\omega(T, r, z) = \frac{J_{\lambda_1}(r, z)}{\kappa_{\lambda_1}(r, z)} \frac{\kappa_{\lambda_2}(r, z)}{J_{\lambda_2}(r, z)} \tag{14}$$

For the area displaying the higher signal level, i.e. the region encompassing $6 < f_v < 8$ ppm, like in Ref. [40], the absolute calibration factor γ_λ is determined at 645 nm from the temperature field of the ratio 580/645. For this couple of spectral ranges, neglecting scattering is believed to be acceptable. Consequently, the field of temperature presented in the following comes from Eq. (11). More information about the calibration method can be found in the Supplementary Material.

Experimental temperature fields have been retrieved for the flames E03-E10 and are displayed in Fig. 11 (left panels). They are compared to the numerical flames N03-N10 (right panels). The same ROI as in the previous section is applied ($f_v > 0.1$ ppm). The global trends are well-reproduced by the numerical simulations: (i) higher temperature levels in the wing and at the flame tip, (ii) a decreasing temperature with increasing pressure. Concerning the absolute values, the experimental ones are systematically higher, to a more pronounced extent at lower pressure.

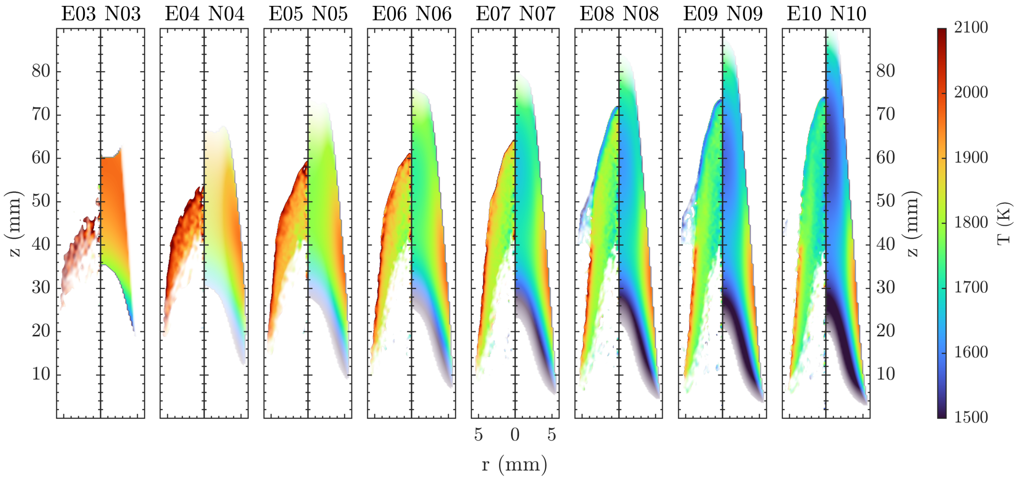

Figure 11: Experimental (left panels) and numerical (right panels) temperature fields of the Region of Interest (ROI) defined by $f_v > 0.1$. For $0.1 < f_v < 0.3$ ppm, transparency is added.

Further examining the thermal topology, Fig. 12 presents the cumulative ROI population of the experimental (left) and numerical (right) temperature fields as a function of pressure. The marker corresponds to the median temperature T_{med}. This figure confirms the temperature decreases as pressure increases, as well as the good agreement between experimental and numerical data. Concerning the median temperatures T_{med}, the evolution is monotonic. Experimentally, this temperature varies from 2010 K for the E03 flame to 1740 K for the E10 flame, i.e. a drop of 270 K. The T amplitude of the variation predicted by the model is higher, with a drop of 320 K.

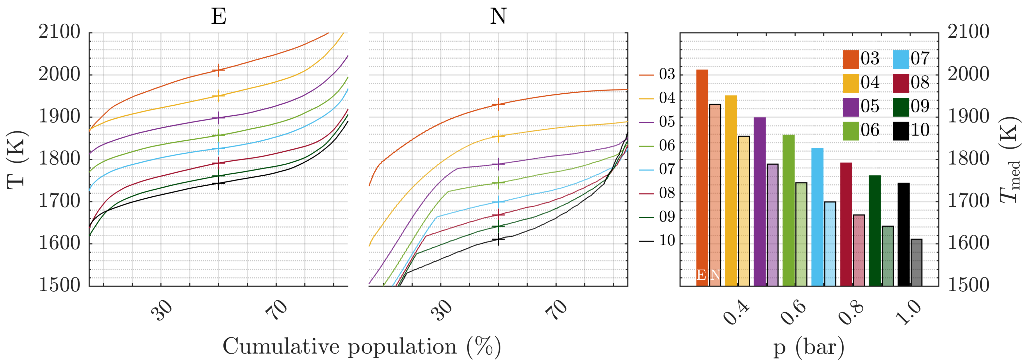

Figure 12: Experimental (left) and numerical (middle) cumulative population and evolution of the median temperature T_{med} with the pressure (right). The marker is the median temperature T_{med}. The numerical median temperatures T_{med} are the bars with the black edges.

Since the temperature decreases with increasing pressure, it seems that any increase in heat release is strongly counter-acted by radiative heat losses. The numerical volume fraction fields f_v overestimating the real concentrations, the radiative losses calculated by CoFlame are then too important. For the same reason, the numerical sooting wings extending higher, the highest locations will potentially reach lower temperatures.

4.2.3. Radiative heat losses

To confirm the increase of radiative heat losses, two quantities can be computed, i.e. the total radiated fraction ζ_{tot} and the soot radiated fraction ζ. The total radiated fraction of the flame power is defined in Eq. (15). The numerator is the power lost by radiative transfer while the denominator is the potential chemical power of the flame, i.e. the ethylene lower heating value $[LHV_{\mathrm{C_2H_4}}]$ times the ethylene mass flow rate $\dot{m}$.

$$\zeta_{tot} = \frac{-S_{q^R}}{[LHV_{\mathrm{C_2H_4}}]\dot{m}_{\mathrm{C_2H_4}}} \tag{15}$$

with $[LHV_{C_2H_4}]$ equal to 47.195 MJ/kg, $\dot{m}_{C_2H_4} = 4$ mg/s, and S_{q^R}, the total radiative heat losses, obtained by the integration over the domain's volume of the divergence of radiative flux q^R by soot, H_2O, CO_2, and CO, as defined in Eq. (16).

$$S_{q^R} = \int_R \int_Z 2\pi r z \nabla q^R(r, z)\, dr dz \tag{16}$$

with R and Z the domain encompassing the iso-contour of the soot volume fraction f_v>0.1 ppm since numerical volume extends farther than the flame's contour.

This quantity cannot be retrieved experimentally, since the contribution of H_2O, CO_2, and CO are unknown. However, even if the contribution of soot to the local radiative heat losses is not straightforward as soot both emits and re-absorbs, its order of magnitude can be illustrated with the field of local emission potential that is derived from the optically thin approximation [2]. In such a case, the local balance of radiative flux attributed to soot only can be basically evaluated provided the knowledge of local soot volume fraction and temperature as follows:

$$\nabla q^R = 4C\sigma f_v T^5 \tag{17}$$

where the value of the constant C is 1.307×10^3 $m^{-1}K^{-1}$ [64], and σ, the Stephan–Boltzmann constant ($5.67\times10^{-8} m^{-2}K^{-4}$). This formulation of the source term may slightly underestimate the soot radiative losses in the hottest regions [64], and supposes the flame is optically thin over distances in the order of the voxel (volume of a pixel) size. However, it allows a straightforward evaluation from soot volume fraction and temperature and enables the evaluation of either experiment or numerical fraction ζ of soot radiation. Additionally, as showed in the Supplementary Material, this quantity has been retrieved numerically from CoFlame and the consistency between the evaluation by Discrete Ordinate Method and Eq. (17) is excellent.

The evolution of the numerical total radiated fraction ζ_{tot} and the soot radiated fractions ζ (experimentally and numerically) with the pressure are presented in Fig. 13. Over this range of pressure, both quantities increase linearly with pressure. The total radiated fraction ζ_{tot} increases from 2% at 0.2 bar to 17% at 1 bar, i.e. a slope of roughly 15%/bar. On the other hand, the soot radiated fractions ζ increases both numerically and experimentally with a slope of roughly 17%/bar, leading to an increase of the soot contribution to the radiative heat losses. Since the experimental flames are smaller than the numerical ones, it is expected that the fractions integrated over the volume are lower.

This result is consistent with the trend observed on temperature, underlying the significant effect of soot concentration on temperatures and consequently flows within the flame. However, it cannot explain the increase of the flame's height with pressure.

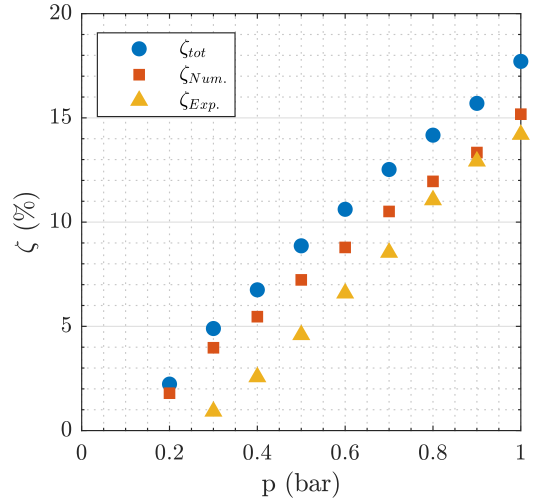

Figure 13: Radiated fraction ζ of the flame power as a function of the pressure.

4.3. Dispersion exponent field

It is commonly assumed that the absorption coefficient of soot is proportional to the inverse of the wavelength at power α [42, 43, 48, 65, 66]:

$$\kappa_\lambda \propto \lambda^{-\alpha} \tag{18}$$

Therefore, measuring the absorption over spectral ranges, we can easily calculate the value of α. To do so, the slope of the linear regression of $\log(\lambda) = f(\log(\kappa_\lambda))$ for the 4 wavelengths λ considered.

The dispersion exponent α can be related to the maturity of the soot [42, 43]. The lower it is, the more mature the soot would be, i.e. large aggregates with graphitic internal spherule structure.

Fig. 14 presents the α fields for the flames E04-E10 with the same ROI than the previous section (f_v>0.1 ppm) (flame E03 is not presented as experimental data are too noisy). The gray lines are streamlines (obtained numerically) that cross either the area where the volume fraction f_v is highest or areas closer to the symmetry axis. The white to red markers along the streamlines represent the travel time t of a particle (from $z = 0$) spaced every 10 ms.

Concerning these streamlines, firstly, it should be noted that the agreement between experimental and numerical fields decaying for lower pressure levels, the streamlines used reflect to a poorer extent the conditions met along the actual streamlines. Secondly, as the pressure decreases the velocities along streamlines increase, consistently with the temperature fields.

This finding is even more striking that it contradicts the initial intuition based on the fact that increasing pressure increases both chemical reaction rates and buoyancy-driven convective flow. In such case, the expanding hot gases would accelerate more rapidly, increasing gas velocities and enhancing the transport of fresh oxidizer to the reaction zone. Furthermore, this finding also differs from Liu et al. [37] numerical results where residence time was found pressure-independent in non-premixed methane flame at pressures ranging from 5 to 40 atmospheres.

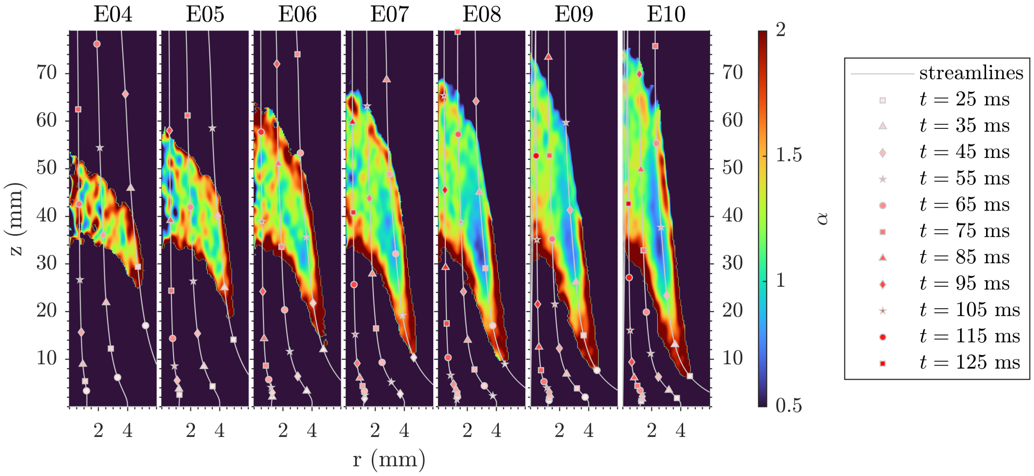

Figure 14: Fields of the dispersion exponent α as a function of the pressure. 3 streamlines are represented in gray. Markers along these lines are spaced by 10 ms.

Several comments can be made regarding this figure. First, all streamlines first encounter high α values, which is consistent since particles must necessarily be formed and then grow before they can mature. Moreover, we observe for almost all conditions, high α values at the boundary between oxidant and fuel, where the oxidation is most intense. Then, overall α decreases with pressure,a finding that the following section addresses.

5. Discussion

Consistently with Ref. [31], as the pressure increases, both the formation time t_f and the oxidation one t_{ox} increase (cf. definition in Section 3.3), f_v increases and the dispersion coefficient α decreases during t_f. Fig. 15 illustrates the increase in residence time with pressure for the streamline passing through the flame wing. On the left side of Fig. 15, the evolution of f_v with pressure and travel time is shown. The insert displays the residence time ($t_r = t_f + t_{ox}$) for each of the pressure levels. On the right side, the dispersion exponent is also represented as a function of time and pressure. The insert displays the minimum value of α for each pressure. We can see that the formation time t_f increases by 23 ms (and t_{ox} increases by 13 ms) between the flame E04 ($t_f = 4$ ms) and the flame E10 ($t_f = 27$ ms). The decrease in α_{min} is 0.8 between the flame E04 ($\alpha_{min} = 1.5$) and the flame E10 ($\alpha_{min} = 0.7$).

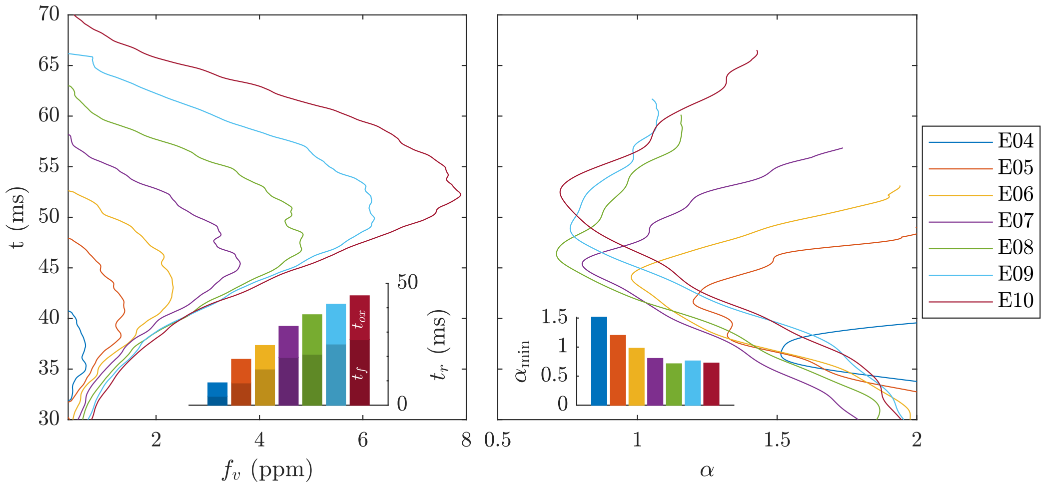

Figure 15: Temporal evolution of the soot volume fraction f_v (left) and the dispersion exponent α (right) over the outermost streamline as a function of the pressure.

These trends are consistent with the results found in Refs. [42, 62] where dilute ethylene flames were studied. To some extent, analogies can be made to explain the results obtained. In the aforementioned references, increasing the dilution of ethylene by nitrogen results in flames generating smaller amounts of soot, with higher temperatures, shorter residence times, and reduced flame heights, i.e. the same effects as the pressure drop in our case.

To our understanding of the phenomena, the increase in residence time can in any case be attributed to lower velocities and higher flames.

The residence time greatly controls the maximum concentration of soot that can be reached. This time is impacted, on the one hand, by the oxygen diffusion and, on the other hand, by the local velocity, itself depending on the local temperature. The increase of the volume fraction is systematically associated with a decrease of the dispersion exponent, suggesting that this one is a good indicator of the soot maturity. The flame height H_f also seems to depend on the soot content, since at constant mass flow rate, the flame height, as well as the propensity to produce soot, increases with pressure. This suggests that the flame height increases due to the longer time needed for the total oxidation of the soot particles in the case of closed flames.

6. Conclusions

Following the MAE procedure, 2D mappings of volume fraction, temperature, and soot dispersion exponent were obtained at constant mass flow rates in non-premixed ethylene/air flames established at a pressure ranging from 0.2 bar to 1 bar. The same flames were studied numerically with CoFlame.

From the f_v volume fraction fields, we established that $f_{v,max}$ evolves with pressure to the power of 2.4 over the range of 0.2 to 1 bar. The increase in pressure leads to a decrease in soot temperature of up to 270 K under our conditions (E03-E10). The augmentation of the formation time t_f (from 4 to 27 ms between E04 and E10, respectively) leads to both higher levels of f_v and higher soot maturity.

Concerning the flame height, as pressure is increased measured soot volume fractions increase since the flame narrows and soot must flow through a smaller cross-section. The increase of soot volume fractions leads to the growth of soot particles which seems to lead to particles more difficult to oxidize (cf. Fig. 15). Furthermore, this growth is associated with the increase of radiative losses (cf. Fig. 13), resulting in lower local temperature levels (cf. Fig. 11) and, consequently, lower flow velocities (cf. Fig. 14). These lower velocities slow the entrainment of fresh oxidizer into the flame, promoting pyrolysis, delaying soot oxidation, and thus stretching vertically the zone favourable to the formation of soot (cf. Fig. 6).

Concerning the comparison between numerical and experimental fields, CoFlame reproduces well the main trends attributed to the pressure. However, it overestimates the level of $f_{v,max}$ for low-pressure conditions. For all flames, the simulation results show trailing wings that extend higher than the experimental measurements. In addition, the soot volume fraction of the flame core above $f_{v,max}$ is systematically underestimated. These differences lead to an overestimation of the radiative losses and incidentally to lower temperatures. These observations suggest potential improvements to the numerical model, both for the soot formation pathways, to improve the agreement of the volume fraction fields along the flame axis, and for the oxidation mechanisms, to resolve the observed disagreements in the upper part of the flame. The large amount of experimental data presented in this work could provide baseline data for validation of numerical modeling.

As numerical perspectives, a numerical equivalent to α would help the comparison of soot maturity between experimental measurement and numerical prediction. Besides, considering reactions inside fuel tube or a modification of the outlet fuel temperature by an iterative process could improve the reproduction of the variation of flame height and the dynamics on $f_{v,max}$ location.

As experimental perspectives, a more sensitive diagnostic could complete f_v of the low pressure cases. Soot sampling could also give valuable assets about soot morphology and maturity.

Acknowledgements

For the financial supports, the authors feel grateful to the Agence Nationale de la Recherche, France (Appibio Project ANR-14-CE22-0003) and to the Centre National d'Etudes Spatiales, France (Contract No. 130615).

References

[1] N. Panek, M. R. J. Charest, L. Gülder, Simulation of Microgravity Diffusion Flames Using Sub-Atmospheric Pressures, AIAA Journal 50 (2012) 976–980.

[2] A. Guibaud, J.-M. Citerne, J.-L. Consalvi, O. Fujita, J. Torero, G. Legros, Experimental Evaluation of Flame Radiative Feedback: Methodology and Application to Opposed Flame Spread Over Coated Wires in Microgravity, Fire Technol. 56 (2020) 185–207.

[3] W. L. Flower, C. T. Bowman, Soot production in axisymmetric laminar diffusion flames at pressures from one to ten atmospheres, Symp. (Int.) Combust. (1988) 1115–1124.

[4] M. Nagachi, J.-M. Citerne, H. Dutilleul, A. Guibaud, G. Jomaas, G. Legros, N. Hashimoto, O. Fujita, Effect of ambient pressure on the extinction limit for opposed flame spread over an electrical wire in microgravity, P. Combust. Inst. 38 (2021) 4767–4774.

[5] W. Lee, Y. D. Na, Soot Study in Laminar Diffusion Flames at Elevated Pressure Using Two-Color Pyrometry and Abel Inversion, JSME Int. J. B-Fluid T. 43 (2000) 550–555.

[6] L. L. McCrain, W. L. Roberts, Measurements of the soot volume field in laminar diffusion flames at elevated pressures, Combust. Flame 140 (2005) 60–69.

[7] K. A. Thomson, L. Gülder, E. J. Weckman, R. A. Fraser, G. J. Smallwood, D. R. Snelling, Soot concentration and temperature measurements in co-annular, nonpremixed CH4/air laminar flames at pressures up to 4 MPa, Combust. Flame 140 (2005) 222–232.

[8] D. S. Bento, K. A. Thomson, L. Gülder, Soot formation and temperature field structure in laminar propane–air diffusion flames at elevated pressures, Combust. Flame 145 (2006) 765–778.

[9] H. I. Joo, L. Gülder, Soot formation and temperature field structure in co-flow laminar methane–air diffusion flames at pressures from 10 to 60atm, P. Combust. Inst. 32 (2009) 769–775.

[10] H. I. Joo, L. Gülder, Soot formation and temperature structure in small methane–oxygen diffusion flames at subcritical and supercritical pressures, Combust. Flame 157 (2010) 1194–1201.

[11] L. Gülder, G. Intasopa, H. I. Joo, P. M. Mandatori, D. S. Bento, M. E. Vaillancourt, Unified behaviour of maximum soot yields of methane, ethane and propane laminar diffusion flames at high pressures, Combust. Flame 158 (2011) 2037–2044.

[12] P. M. Mandatori, L. Gülder, Soot formation in laminar ethane diffusion flames at pressures from 0.2 to 3.3MPa, P. Combust. Inst. 33 (2011) 577–584.

[13] E. A. Griffin, L. Gülder, Soot formation in diluted laminar ethene, propene and 1-butene diffusion flames at elevated pressures, Combust. Flame 197 (2018) 378–388.

[14] H. Kwon, A. Jain, C. S. McEnally, L. D. Pfefferle, Y. Xuan, Numerical investigation of the pressure-dependence of yield sooting indices for n-alkane and aromatic species, Fuel 254 (2019) 115574.

[15] I. Ruiz-Rodriguez, R. Cracknell, M. Parkes, T. Megaritis, L. Ganippa, Experimental study of the effect of C8 oxygenates on sooting processes in high pressure spray flames, Combust. Flame 220 (2020) 235–246.

[16] S. S. Yang, L. Gülder, Pressure dependence of sooting characteristics of m-xylene and n-octane doped laminar methane diffusion flames from 2 to 10 bar, Combust. Flame 220 (2020) 203–209.

[17] P. Liu, C. Chu, I. Alsheikh, S. R. Gubba, S. Saxena, O. Chatakonda, J. W. Kloosterman, F. Liu, W. L. Roberts, Soot production in high pressure inverse diffusion flames with enriched oxygen in the oxidizer stream, Combust. Flame 245 (2022) 112378.

[18] G. Intasopa, Soot Measurements in High-pressure Diffusion Flames of Gaseous and Liquid Fuels, Thesis, University of Toronto (2011).

[19] A. E. Karataş, L. Gülder, Soot formation in high pressure laminar diffusion flames, Prog. Energ. Combust. 38 (2012) 818–845.

[20] M. D. Smooke, C. S. McEnally, L. D. Pfefferle, R. J. Hall, M. B. Colket, Computational and experimental study of soot formation in a coflow, laminar diffusion flame, Combust. Flame 117 (1999) 117–139.

[21] F. Liu, H. Guo, G. J. Smallwood, L. Gülder, Numerical modelling of soot formation and oxidation in laminar coflow non-smoking and smoking ethylene diffusion flames, Combust. Theor. Model. 7 (2003) 301–315.

[22] C. W. Lautenberger, J. L. de Ris, N. A. Dembsey, J. R. Barnett, H. R. Baum, A simplified model for soot formation and oxidation in CFD simulation of non-premixed hydrocarbon flames, Fire Safety J. 40 (2005) 141–176.

[23] G. Blanquart, H. Pitsch, Analyzing the effects of temperature on soot formation with a joint volume-surface-hydrogen model, Combust. Flame 156 (2009) 1614–1626.

[24] T. Beji, J. P. Zhang, W. Yao, M. Delichatsios, A novel soot model for fires: Validation in a laminar non-premixed flame, Combust. Flame 158 (2011) 281–290.

[25] N. A. Eaves, Q. Zhang, F. Liu, H. Guo, S. B. Dworkin, M. J. Thomson, CoFlame: A refined and validated numerical algorithm for modeling sooting laminar coflow diffusion flames, Comput. Phys. Commun. 207 (2016) 464–477.

[26] A. Mansouri, N. A. Eaves, M. J. Thomson, S. B. Dworkin, Influence of pressure on near nozzle flow field and soot formation in laminar co-flow diffusion flames, Combust. Theor. Model. 23 (2019) 536–548.

[27] A. Mansouri, L. Zimmer, S. B. Dworkin, N. A. Eaves, Impact of pressure-based HACA rates on soot formation in varying-pressure coflow laminar diffusion flames, Combust. Flame 218 (2020) 109–120.

[28] M. Sun, Z. Gan, A Numerical Study on the Influence of Hydrogen Addition on Soot Formation in a Laminar Aviation Kerosene (Jet A1) Flame at Elevated Pressure, ASME Turbo Expo, 2021.

[29] J. J. Warchol, J. J. Reuther, Effect of Sub-Atmospheric Pressure on Soot and Hydroxyl Concentrations in Quenched, Premixed Ethane/Air Flat Flames, Combust. Sci. Techno.l 38 (1984) 325–336.

[30] C. H. Kim, A. M. El-Leathy, F. Xu, G. M. Faeth, Soot surface growth and oxidation in laminar diffusion flames at pressures of 0.1–1.0 atm, Combust. Flame 136 (2004) 191–207.

[31] M. R. J. Charest, C. P. T. Groth, L. Gülder, A numerical study on the effects of pressure and gravity in laminar ethylene diffusion flames, Combust. Flame 158 (2011) 1933–1945.

[32] H. Li, Z. Zhou, Y. Niu, J. Yao, D. Zhou, J. Wang, Effect of Pressure and Type of Fuel on Laminar Diffusion Flame Height at Subatmospheric Pressures, Chem. Technol. Fuels Oils 51 (2015) 389–396.

[33] J. Fang, J.-W. Wang, J.-F. Guan, Y.-M. Zhang, J.-J. Wang, Momentum- and buoyancy-driven laminar methane diffusion flame shapes and radiation characteristics at sub-atmospheric pressures, Fuel 163 (2016) 295–303.

[34] M. R. J. Charest, C. P. T. Groth, L. Gülder, Effects of gravity and pressure on laminar coflow methane–air diffusion flames at pressures from 1 to 60 atmospheres, Combust. Flame 158 (5) (2011) 860–875.

[35] I. M. Miller, H. G. Maahs, High pressure flame system for pollution studies with results for methane-air diffusion flames, Tech. rep., NASA (1977).

[36] I. Glassman, Sooting laminar diffusion flames: Effect of dilution, additives, pressure, and microgravity, Symp. (Int.) Combust. 27 (1) (1998) 1589–1596.

[37] F. Liu, K. A. Thomson, H. Guo, G. J. Smallwood, Numerical and experimental study of an axisymmetric coflow laminar methane–air diffusion flame at pressures between 5 and 40 atmospheres, Combust. Flame 146 (2006) 456–471.

[38] F. G. Roper, The prediction of laminar jet diffusion flame sizes: Part I. Theoretical model, Combust. Flame (1977) 219–226.

[39] T. P. Jenkins, R. K. Hanson, Soot pyrometry using modulated absorption/emission, Combust. Flame 126 (2001) 1669–1679.

[40] G. Legros, Q. Wang, J. Bonnety, M. Kashif, C. Morin, J.-L. Consalvi, F. Liu, Simultaneous soot temperature and volume fraction measurements in axis-symmetric flames by a two-dimensional modulated absorption/emission technique, Combust. Flame 162 (2015) 2705–2719.

[41] J. Bonnety, A. Guibaud, R. Jalain, A. Matynia, J.-L. Consalvi, F. Liu, G. Legros, Probing the local radiative quenching during the transition from a non-smoking to a smoking laminar coflow ethylene/air nonpremixed flame, Combust. Flame 203 (2019) 120–129.

[42] N. J. Kempema, B. Ma, M. B. Long, Investigation of in-flame soot optical properties in laminar coflow diffusion flames using thermophoretic particle sampling and spectral light extinction, Appl. Phys. B 122 (2016) 232.

[43] J. Yon, J. J. Cruz, F. Escudero, J. Morán, F. Liu, A. Fuentes, Revealing soot maturity based on multi-wavelength absorption/emission measurements in laminar axisymmetric coflow ethylene diffusion flames, Combust. Flame 227 (2021) 147–161.

[44] F. P. Hagen, D. Kretzler, S. Koch, H. Bockhorn, R. Suntz, D. Trimis, H. Kubach, A. Velji, T. Koch, On-line monitoring of carbon nanostructure and soot reactivity in engine exhaust by dual-pulse laser-induced incandescence, Combust. Flame 254 (2023) 112850.

[45] H. Li, Y. He, J. Wang, Determination of Smoke Point of Laminar Acetylene Diffusion Flames Under Subatmospheric Pressures, Combust. Sci. Technol. 186 (2014) 1237–1248.

[46] R. L. Vander Wal, A. J. Tomasek, Soot oxidation: dependence upon initial nanostructure, Combust. Flame 134 (2003) 1–9.

[47] J. Camacho, Y. Tao, H. Wang, Kinetics of nascent soot oxidation by molecular oxygen in a flow reactor, P. Combust. Inst. 35 (2015) 1887–1894.

[48] K. O. Johansson, F. El Gabaly, P. E. Schrader, M. F. Campbell, H. A. Michelsen, Evolution of maturity levels of the particle surface and bulk during soot growth and oxidation in a flame, Aerosol Sci. Tech. 51 (2017) 1333–1344.

[49] J. Davis, E. Molnar, I. Novosselov, Nanostructure transition of young soot aggregates to mature soot aggregates in diluted diffusion flames, Carbon 159 (2020) 255–265.

[50] C. S. McEnally, L. D. Pfefferle, The effects of dimethyl ether and ethanol on benzene and soot formation in ethylene nonpremixed flames, P. Combust. Inst. 31 (2007) 603–610.

[51] C. S. McEnally, L. D. Pfefferle, Sooting Tendencies of Oxygenated Hydrocarbons in Laboratory-Scale Flames, Environ. Sci. Technol. 45 (2011) 2498–2503.

[52] S. Karnani, D. Dunn-Rankin, Visualizing CH* chemiluminescence in sooting flames, Combust. Flame 160 (2013) 2275–2278.

[53] N. A. Slavinskaya, P. Frank, A modelling study of aromatic soot precursors formation in laminar methane and ethene flames, Combust. Flame 156 (2009) 1705–1722.

[54] M. Frenklach, H. Wang, Detailed modeling of soot particle nucleation and growth, Symp. (Int.) Combust. 23 (1) (1991) 1559–1566.

[55] J. Appel, H. Bockhorn, M. Frenklach, Kinetic modeling of soot formation with detailed chemistry and physics: laminar premixed flames of C2 hydrocarbons, Combust. Flame 121 (1) (2000) 122–136.

[56] K. G. Neoh, J. B. Howard, A. F. Sarofim, Soot Oxidation in Flames, in: D. C. Siegla, G. W. Smith (Eds.), Particulate Carbon: Formation During Combustion, Springer US, Boston, MA, 1981, pp. 261–282.

[57] H. Guo, P. M. Anderson, P. B. Sunderland, Optimized rate expressions for soot oxidation by OH and O2, Fuel 172 (2016) 248–252.

[58] F. Liu, G. J. Smallwood, O. L. Gülder, Band Lumping Strategy for Radiation Heat Transfer Calculations Using a Narrowband Model, J. Thermophys. Heat Tr. 14 (2) (2000) 278–281.

[59] M. Kashif, P. Guibert, J. Bonnety, G. Legros, Sooting tendencies of primary reference fuels in atmospheric laminar diffusion flames burning into vitiated air, Combust. Flame 161 (2014) 1575–1586.

[60] H.-C. Chang, T. T. Charalampopoulos, Determination of the wavelength dependence of refractive indices of flame soot, P. Roy. Soc. Lond. A Mat. 430 (1990) 577–591.

[61] R. J. Santoro, H. G. Semerjian, R. A. Dobbins, Soot particle measurements in diffusion flames, Combust. Flame 51 (1983) 203–218.

[62] M. D. Smooke, M. B. Long, B. C. Connelly, M. B. Colket, R. J. Hall, Soot formation in laminar diffusion flames, Combust. Flame 143 (2005) 613–628.

[63] A. E. Karataş, L. Gülder, Dependence of sooting characteristics and temperature field of co-flow laminar pure and nitrogen-diluted ethylene–air diffusion flames on pressure, Combust. Flame 162 (2015) 1566–1574.

[64] S. J. Brookes, J. B. Moss, Predictions of soot and thermal radiation properties in confined turbulent jet diffusion flames, Combust. Flame 116 (1999) 486–503.

[65] M. F. Modest, Radiative Heat Transfer, 2nd Edition, Boston: Academic Press, Academic Press, 2003.

[66] K. Gleason, F. Carbone, A. Gomez, Effect of temperature on soot inception in highly controlled counterflow ethylene diffusion flames, Combust. Flame 192 (2018) 283–294.